



Ab initio study of ultrafast demagnetization of elementary ferromagnets by terahertz versus optical pulses

Camilla Pellegrini ^{1,*}, Sangeeta Sharma,² John Kay Dewhurst,³ and Antonio Sanna ³

¹*Dipartimento di Fisica e Geologia, Università di Perugia, Via Pascoli 33, 06123 Perugia, Italy*

²*Max-Born-Institut für Nichtlineare Optik und Kurzzeitspektroskopie, Max-Born-Strasse 2A, 12489 Berlin, Germany*

³*Max-Planck-Institut für Mikrostrukturphysik, Weinberg 2, D-06120 Halle, Germany*



(Received 9 March 2022; revised 9 April 2022; accepted 11 April 2022; published 20 April 2022)

We present an *ab initio* time-dependent density functional theory study of the ultrafast demagnetization of elemental ferromagnets subject to terahertz (THz) laser pumping compared to optical laser pumping. We find that THz radiation can cause as much demagnetization as optical radiation for significantly lower-energy transfer to the sample. We show that the demagnetization efficiency of the THz pulse is related to a coherent coupling of the radiation to the electron charge dynamics. In fact, our simulations reveal that the low-frequency THz electric field enforces in-phase electron charge oscillations around the atomic centers, leading to a highly efficient spin-orbit torque switching of the magnetization. Unlike for optical pumping, at the end of the pulse a major fraction of the excited electrons is driven back to equilibrium acquiring a thermalized Fermi-Dirac distribution.

DOI: [10.1103/PhysRevB.105.134425](https://doi.org/10.1103/PhysRevB.105.134425)

I. INTRODUCTION

Understanding the ultrafast response of magnetic materials to light perturbation is of crucial importance to improve data storage technology and boost spin electronics [1,2]. Past investigations have extensively focused on the ultrafast demagnetization dynamics induced by optical laser pulses. [3–5]. In these experiments, the energy transfer to the sample gives rise to a strongly nonthermal electron distribution, leading, within a short time (~ 100 fs), to incoherent quenching of the magnetization [6]. In order to achieve better control over the spin dynamics, experimental interest has lately shifted towards terahertz (THz) radiation [7]: In contrast to visible light, which carries excessive photon energy, THz light can resonantly excite spin precessions on the low-frequency (meV) scale. Coherent precessional spin motion driven by the THz magnetic field has been reported by several studies in the low pump fluence regime [8,9]. Importantly, the recent availability of strong few-cycle THz pulses has opened the path towards precessional magnetization switching, which would increase the current speed of data processing. First results on transition metal ferromagnets show, however, that the spin dynamics at high field intensities is dominated by a large incoherent magnetization quenching, similar to that observed after optical pumping [9,10].

Several mechanisms have been addressed as (co)responsible for angular momentum transfer among the laser, electronic, and lattice degrees of freedom, such as spin-flip scattering at (quasi-)particles or impurities [11,12] and spin-polarized transport [13]. To date, not all the proposed mechanisms are within reach of *ab initio* methods, and, therefore, their investigation needs to rely on strong assumptions or empirical evidence, leaving space for many

open controversies [5]. *Ab initio* time-dependent density functional theory [14,15] (TDDFT) is a rigorous framework to describe electron and spin dynamics driven by external electromagnetic fields and has shown to be accurate at very short timescales before lattice vibrations and complex electronic and spin correlations set in. In particular, TDDFT calculations have highlighted the crucial role played by the spin-orbit coupling (SOC) in the early stages of the optically induced demagnetization process [16]. In this paper, we simulate the interaction of a strong single-cycle THz pulse with the elemental bulk ferromagnets Fe, Co, and Ni by means of TDDFT, to achieve a full first-principles description of the ultrafast demagnetization dynamics and compare it to that by optical pulses with the same wave packet.

II. METHODOLOGY

TDDFT generalizes the one-to-one density-potential mapping of ground state DFT to the time domain. Based on this mapping, a system of noninteracting particles in an effective potential, the so-called Kohn-Sham (KS) system, can be chosen such as to reproduce the density of the interacting system at all times [17,18]. This enables to construct the time-dependent interacting density from single-particle orbitals. In what follows we employ a noncollinear spin-dependent extension of the theory, which reproduces, in principle exactly, the ultrafast spin dynamics induced in a ferromagnet by a long wavelength electric pulse [16,19,20]. Specifically, the KS orbitals $\psi_j(\mathbf{r}, t)$ are Pauli spinors fulfilling the single-particle time-dependent Schrödinger equations,

$$i \frac{\partial \psi_j(\mathbf{r}, t)}{\partial t} = \left[\frac{1}{2} \left(-i \nabla + \frac{1}{c} \mathbf{A}_{\text{ext}}(t) \right)^2 + v_s(\mathbf{r}, t) + \frac{1}{2c} \boldsymbol{\sigma} \cdot \mathbf{B}_{\text{xc}}(\mathbf{r}, t) + \frac{1}{4c^2} \boldsymbol{\sigma} \cdot (\nabla v_s(\mathbf{r}, t) \times -i \nabla) \right] \times \psi_j(\mathbf{r}, t), \quad (1)$$

*pellegrini.physics@gmail.com

where the last term accounts for the SOC and the exchange correlation (xc). $\mathbf{A}_{\text{ext}}(t)$ is the vector potential of the applied laser field in the dipole approximation, whereas $\mathbf{B}_{\text{xc}}[\rho, \mathbf{m}](\mathbf{r}, t)$ is the effective magnetic field caused by the exchange interaction. The KS electronic potential $v_s[\rho, \mathbf{m}](\mathbf{r}, t) = v_{\text{ext}}(\mathbf{r}, t) + \int \frac{\rho(\mathbf{r}', t)}{|\mathbf{r}-\mathbf{r}'|} d\mathbf{r}' + v_{\text{xc}}[\rho, \mathbf{m}](\mathbf{r}, t)$ consists of the external electric field originating from the nuclei and the laser pulse, the usual Hartree potential, and the xc Coulomb potential. $\mathbf{B}_{\text{xc}}(\mathbf{r}, t)$ and $v_{\text{xc}}(\mathbf{r}, t)$ are universal functionals of the electron density ρ and the magnetization density \mathbf{m} , which are computed as

$$\rho(\mathbf{r}, t) = \sum_{j=1}^N \sum_{\sigma} \psi_{j\sigma}^{\dagger}(\mathbf{r}, t) \psi_{j\sigma}(\mathbf{r}, t), \quad (2)$$

$$\mathbf{m}(\mathbf{r}, t) = \sum_{j=1}^N \sum_{\alpha, \beta} \psi_{j\alpha}^{\dagger}(\mathbf{r}, t) \boldsymbol{\sigma} \psi_{j\beta}(\mathbf{r}, t), \quad (3)$$

where $\boldsymbol{\sigma}$ denotes the 2×2 Pauli matrices and N is the number of occupied states. In this paper we employ for the xc functionals the noncollinear adiabatic local spin-density approximation (ALSDA) [21–23]. Since ALSDA satisfies by construction the zero-torque theorem, the dynamics of the global magnetic moment $\mathbf{M}(t) = \int d^3r \mathbf{m}(\mathbf{r}, t)$ in the absence of external magnetic fields, is solely determined by the SOC, that is

$$\frac{d}{dt} \mathbf{M}(t) = \frac{1}{2c^2} \int d^3r \begin{bmatrix} \hat{x} \\ \hat{y} \\ \hat{z} \end{bmatrix} \begin{bmatrix} \nabla v_s(\mathbf{r}, t) \times \mathbf{j}_x^s(\mathbf{r}, t) \\ \nabla v_s(\mathbf{r}, t) \times \mathbf{j}_y^s(\mathbf{r}, t) \\ \nabla v_s(\mathbf{r}, t) \times \mathbf{j}_z^s(\mathbf{r}, t) \end{bmatrix}, \quad (4)$$

where the spin current density \mathbf{j}^s is related to the usual current density through $\mathbf{j}^s = \boldsymbol{\sigma} \otimes \mathbf{j}$. In order to gain deeper insights into the processes driven by the excitation pulse, a time-dependent generalization of the density of states (DOS) concept is introduced [24]. The time-dependent DOS is defined as

$$\text{DOS}(\omega, t) = \sum_{ijk} \delta(\omega - \epsilon_{ik}) n_{jk} |O_{ijk}(t)|^2, \quad (5)$$

where n_{jk} is the KS-orbital occupation number and

$$O_{ijk}(t) = \int d^3r \psi_{ik}^*(\mathbf{r}, 0) \psi_{jk}(\mathbf{r}, t) \quad (6)$$

is the projection of the generic time-dependent KS orbital onto the initial ground-state orbitals.

Computational details

Simulations are performed within periodic boundary conditions by assuming the dipole approximation for the radiation. The lattice is assumed to be perfect and periodic and is kept fixed at its equilibrium structure. Electron-phonon and electron-impurity interaction effects are, therefore, neglected, and so is the possibility of phonon- and impurity-driven Elliott-Yafet demagnetization [11,12]. TDDFT simulations are carried out based on Eq. (1) as implemented in the all-electron ELK code [25] by employing noncollinear ALSDA. The time propagation is performed using the algorithm presented in Ref. [26] with a time step of 0.242 as.

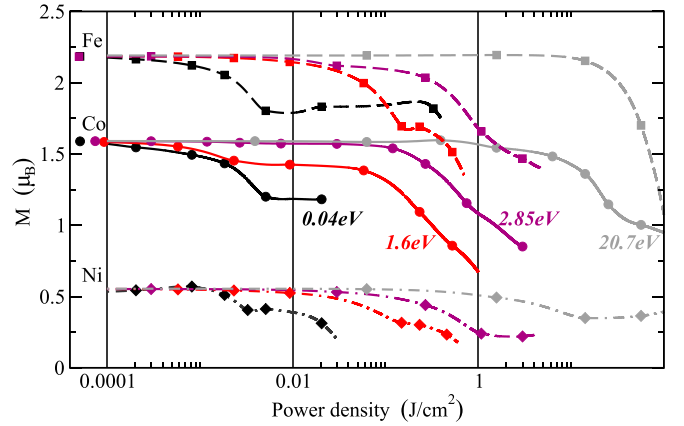


FIG. 1. Atomic magnetic moment of bulk Fe (squares), Co (circles), and Ni (diamonds) at 100 fs after the pulse peak as a function of the pump fluence. Black, red, violet, and gray points refer, respectively, to 10 THz, 780-nm near infrared, 434-nm violet, and 60-nm extreme ultraviolet radiation. Lines are a guide to the eye.

The ELK code basis set consists of linearized augmented plane waves [27], which decompose the system into so-called muffin-tin regions centered on each atom, and the interstitial region in between them. The lattice parameters used for Fe (bcc), Co (fcc), and Ni (fcc) are 2.87, 3.54, and 3.52 Å, respectively. We adopt a smearing width of 5 mHa for the ground-state orbital occupations. The Brillouin zone is accurately sampled with a 16^3 \mathbf{k} grid. Laser pulses are represented by a Gaussian envelope function with a full width at half maximum of 40 fs. We consider the following radiation frequencies: 10 THz (30 000 nm), 385 THz (780-nm near infrared), 690 THz (434-nm violet), and 5000 THz (60-nm ultraviolet).

III. RESULTS AND DISCUSSION

The demagnetization mechanism that we account for in our simulations are spin-flip events driven by SOC [19]. For typical 3d ferromagnets, such as Fe, Co, and Ni, the orbital and spin angular momenta tend to be aligned along the same direction, as d shells are more than half-filled. Under laser excitation, valence electrons are promoted into higher-energy delocalized states with subsequent reduction and change in the orientation of the orbital angular momenta of the atoms. Since spin and orbital motion are coupled, this variation triggers the demagnetization of the remaining d electrons close to the atomic cores where the strength of the SOC [proportional in Eq. (1) to the gradient of the KS potential ∇v_s] is larger. Ultrafast quenching of the magnetization is observed in all the ferromagnets under investigation for both optical and THz pumping. The change in the global magnetic moment of the materials as a function of the laser fluence (energy delivered per unit area) is shown in Fig. 1. As a common trend, the reduction of the magnetic moment becomes stronger at higher fluence until a maximum demagnetization of about 50% is achieved. In the weak-field limit, the THz induced demagnetization increases almost linearly with the laser fluence, in agreement with experimental results [10,28].

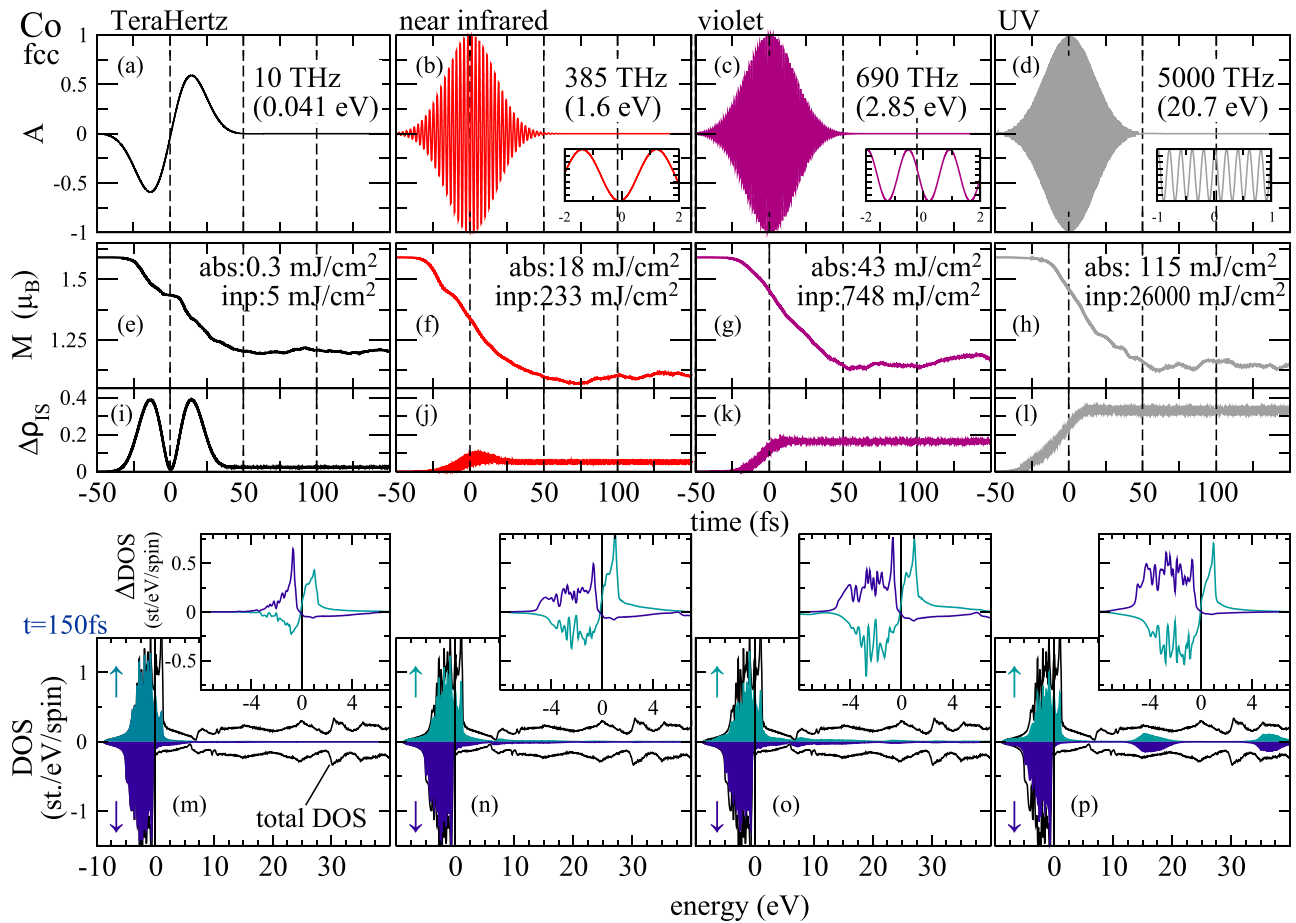


FIG. 2. Demagnetization of bulk Co upon ultrafast excitation. (a)–(d) Normalized intensity profiles of the incident pulses. (e)–(f) Time evolution of the atomic magnetization for given input and absorbed pulse fluences. (i)–(l) Time evolution of the electron charge dislocated by pulse excitation into the interstitial region. (m)–(p) Density of states for the majority and minority spin bands at the final time $t = 150$ fs and (the inset) its deviation from equilibrium. The solid line is the total density of states, whereas colored areas represent the occupied states. Majority spin is plotted on the negative ordinate.

The observed demagnetization is expected to be roughly proportional to the amount of charge that the electric field extracts from regions close to the atomic core. At low-field intensity, high-energy radiation can excite electrons from a large bandwidth, whereas THz radiation can promote electrons within a few meV around the Fermi level. However, our simulations show that at high radiation fluence, that is in the nonlinear regime, the THz pulse is able to empty a large fraction (several eV wide) of the valence band more efficiently than optical radiation. To further investigate this aspect, we compare the effects on bulk Co of laser pulses with selected frequencies (see legend in Fig. 2) and high intensities, chosen to yield approximately the same reduction of the magnetization at saturation (~ 150 fs after the pulse peak). Qualitatively similar results are obtained for Fe and Ni. For each laser pulse, Fig. 2 shows the normalized intensity profile (a)–(d), the induced change in the atomic magnetic moment (e)–(h), and the evolution of the electron population in the interstitial region (i)–(l). The electronic occupied DOS at the final time $t = 150$ fs (m)–(p) and its deviation from the initial ground-state value (in the inset) are also included. We observe that the temporal profile of the magnetization is nearly identical for all the pulse frequencies. This universal

behavior of the magnetization clearly demonstrates that the spin loss is almost unaffected by the excitation photon energy and is mainly determined by the pulse profile and the intrinsic timescale of the spin-orbit mediated demagnetization mechanism.

The main qualitative difference between optical and THz radiation lies in the way charge is extracted from the atomic core region. As optical pulses oscillate at a much faster timescale (\sim fs) than the natural speed of the electronic motion, electrons cannot follow the rapid reversal of the field. The high frequency of the radiation causes vertical electronic transitions as sketched in Fig. 3(a) for the band structure of Co. This is clearly seen in our simulation data for the UV pulse where the final DOS [Fig. 2(p)] presents disjoint pockets of electrons excited to high-energy states. If the radiation energy is smaller than the valence bandwidth, pockets do not form and one observes a single excitation tail [Figs. 2(n) and 2(o)], whose extension in energy depends on both the pump frequency and the fluence. Figure 3(b) shows snapshots of the electron displacement in real space caused by the violet pulse of Fig. 2(c) where areas of charge removal (accumulation) are enclosed by red (yellow) surfaces [29]. Here, electronic excitations increase monotonically during the pulse, leading

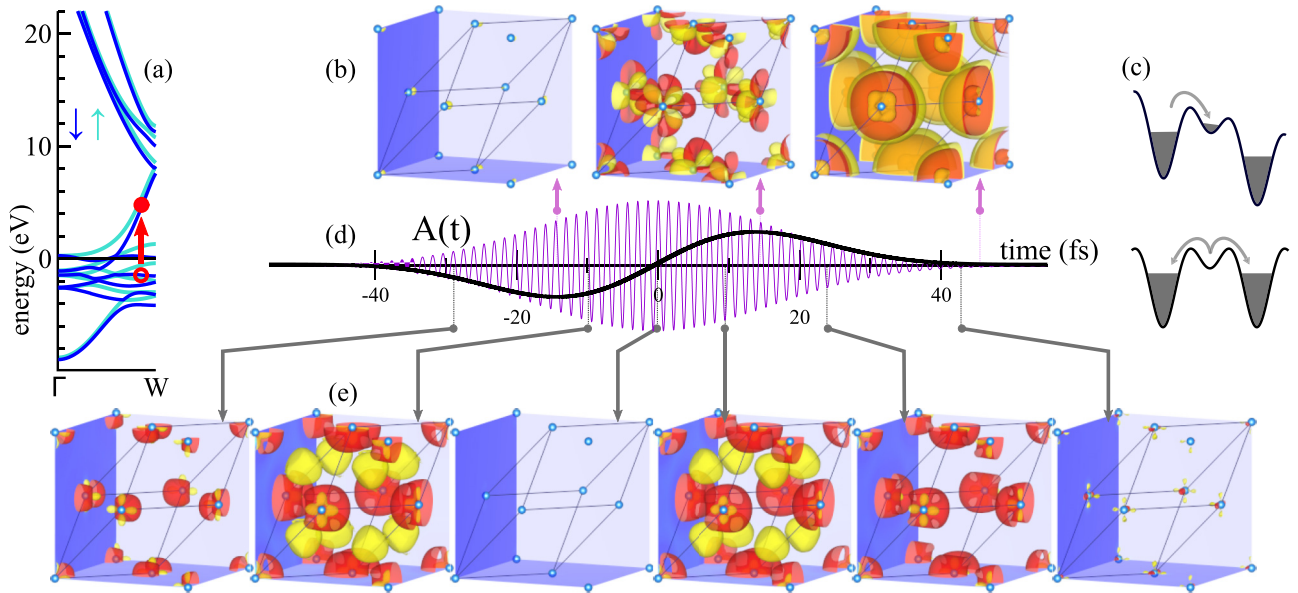


FIG. 3. The effect of optical and THz pulses on ferromagnetic Co. (a) Band structure of Co along the Γ -W line of the Brillouin zone. The rapid oscillations of the vector potential associated with the optical pulse (panel d, purple) cause interband transitions (red arrow). Dark and light blue bands refer to majority and minority spin states. (c) The vector potential of the THz pulse (panel d, black) induces slow deformations of the electrostatic potential, leading to reversible charge transfer to the interatomic region. (b) Computed charge dynamics at $t = -14, 14,$ and 46 fs for the optical pulse, and (e) at $t = -29, -10, 0, 10, 24, 43$ fs for the THz pulse as time snapshots of charge-density difference isosurfaces. Regions of charge depletion and accumulation are red and yellow, respectively. Calculations refer to the 750-mJ/cm^2 violet pulse and to the 5-mJ/cm^2 10-THz pulse of Figs. 2(a) and 2(c).

to changes in the orbital character of the electron density and to the buildup of charge in the interstitial space. On the contrary, THz field oscillations are much slower: In our example the field direction is reversed over ≈ 50 fs. This time is sufficient for the electrons to feel a distorted electrostatic potential and relax accordingly. The process is sketched in Fig. 3(c) and can be followed in time in Fig. 3(e). As the laser is switched on, electrons drift away from the nuclei, and when the electric field is strong enough, can tunnel to non-nuclear attractors located in the interstitial region. Following the inversion of the field, electrons are driven back close to their equilibrium configuration. The process repeats itself in the second half laser cycle. This trend is consistent with Fig. 2(i) where the interstitial electron density oscillates in between a maximum of ~ 0.4 electrons at the inversion points of the electric field and a minimum ~ 0.01 , close to the node of the vector potential.

Even though the majority of the interstitial charge is driven back to the core region at the end of the pulse, SOC-mediated demagnetization occurs very efficiently during the coherent displacement of the electrons. This provides a rationale for why strong THz fields are able to achieve sizable ultrafast demagnetization despite a relatively small final perturbation of the electronic DOS as compared to optical radiation [compare the insets of Figs. 2(m)–2(p)]. In fact, laser-driven charge oscillations become hardly visible for radiation at the low end of the optical spectrum [see the small bump in the profile of the interstitial charge in Fig. 2(j)], and completely disappear at higher frequencies [Figs. 2(k) and 2(l)]. Interestingly, our interpretation is validated by the prediction of a temporary stop in the THz-induced demagnetization dynamics [Fig. 2(d), in

correspondence with the node of the vector potential], which has been experimentally confirmed [28].

We point out that the methodology here employed has shown to well reproduce the early stages of ultrafast optical demagnetization as measured in a number of experiments [19,30–32]. On a scale from ≈ 100 fs to 1 ps, nonthermal electrons are expected to scatter among themselves approaching a hot Fermi-Dirac distribution and then cool down by transferring energy and possibly spin [33] to the lattice via electron-phonon scattering. Relaxation processes, however, are not included in our approach as it would require including electron-phonon interactions and going beyond adiabatic approximations to the xc functional. This is apparent from Fig. 2(p) where the UV pulse generates pockets of hot electrons, which should rapidly scatter and lose energy to other electrons and phonons [34] but appear to be stable. Partly due to this limitation of the functional, simulations for high-frequency laser pulses require larger fluences than those used in experiments. From the data in Figs. 2(n)–2(p), we estimate that a significant fraction of the absorbed optical photon energy (from 60% for infrared radiation up to 95% for UV radiation) gets locked into high-energy electronic states and does not contribute further to the overall spin dynamics of the system. On the other hand, this problem does not seem to occur for THz radiation since high-energy excitations do not develop even at high pump fluence.

By computing the value of reduced χ^2 for the DOS in Fig. 2(m) with respect to the Fermi-Dirac distribution, we find that after THz pumping electrons are still fairly thermal ($\bar{\chi}^2 = 2$). On the other hand, by excitation with infrared and violet pulses, high-energy tail states of the DOS get populated

[Figs. 2(n) and 2(o)] and increasing deviations from thermal behavior appear ($\bar{\chi}^2$ values equal to 3 and 3.3, respectively).

IV. CONCLUSION

By means of first-principles TDDFT simulations, we have investigated the effect of THz laser pumping on elemental magnets and compared it to that of conventional optical pumping. Owing to the nature of the approximations involved, our approach is meant to describe a short timescale after the pump on the order of 100 fs where electron-electron and spin-orbit interactions dominate. Our simulations reveal that in the nonlinear regime THz pulses can induce ultrafast demagnetization very efficiently at much lower-energy transfer to the sample. We identify the underlying demagnetization mechanism to be the same as for optical laser pulses, that is, spin-orbit-mediated spin flip caused by optical excitation of electrons to higher-energy delocalized states. The demagnetization efficiency of the THz pulse is explained by a coherent interaction of the radiation with the electron charge dynamics as the slowly oscillating electric field induces in-phase space modulations of the electron density. At large field intensities,

electrons are accelerated through the valence band up to large kinetic energies (\sim eV). The associated charge current gives rise close to the atomic centers to a large spin torque, which efficiently demagnetizes the sample. This observation suggests that THz-induced magnetization quenching can be effectively tuned in materials by tailoring their electron mobility, or by perturbing the interstitial potential, e.g., by means of partial hydrogenation. Unlike for optical excitation, at the end of the THz pulse, electrons are driven back to a thermalized Fermi-Dirac distribution. As a consequence, the later-time dynamics is expected to be essentially dominated by energy transfer to the lattice via electron-phonon scattering. Our results suggest that an experimental investigation of the sub-100-fs (10–30-THz) pump regime would be of utmost interest to assess the relative contributions of electronic relaxation processes and lattice scattering to ultrafast demagnetization.

ACKNOWLEDGMENTS

S.S. and J.K.D. thank DFG for funding through Project-ID 328545488 - TRR 227, Project No. A04. C.P. acknowledges financial support from the CarESS Project.

-
- [1] D. Sander, S. O. Valenzuela, D. Makarov, C. H. Marrows, E. E. Fullerton, P. Fischer, J. McCord, P. Vavassori, S. Mangin, P. Pirro, B. Hillebrands, A. D. Kent, T. Jungwirth, O. Gutfleisch, C. G. Kim, and A. Berger, *J. Phys. D: Appl. Phys.* **50**, 363001 (2017).
- [2] E. Y. Vedmedenko, R. K. Kawakami, D. D. Sheka, P. Gambardella, A. Kirilyuk, A. Hirohata, C. Binek, O. Chubykalo-Fesenko, S. Sanvito, B. J. Kirby, J. Grollier, K. Everschor-Sitte, T. Kampfrath, C.-Y. You, and A. Berger, *J. Phys. D: Appl. Phys.* **53**, 453001 (2020).
- [3] E. Beaupaire, J.-C. Merle, A. Daunois, and J.-Y. Bigot, *Phys. Rev. Lett.* **76**, 4250 (1996).
- [4] B. Koopmans, M. van Kampen, J. T. Kohlhepp, and W. J. M. de Jonge, *Phys. Rev. Lett.* **85**, 844 (2000).
- [5] A. Kirilyuk, A. V. Kimel, and T. Rasing, *Rev. Mod. Phys.* **82**, 2731 (2010).
- [6] T. Roth, A. J. Schellekens, S. Alebrand, O. Schmitt, D. Steil, B. Koopmans, M. Cinchetti, and M. Aeschlimann, *Phys. Rev. X* **2**, 021006 (2012).
- [7] T. Kampfrath, K. Tanaka, and K. A. Nelson, *Nat. Photonics* **7**, 680 (2013).
- [8] C. Vicario, C. Ruchert, F. Ardana-Lamas, P. M. Derlet, B. Tudu, J. Luning, and C. P. Hauri, *Nat. Photonics* **7**, 720 (2013).
- [9] M. Shalaby, A. Donges, K. Carva, R. Allenspach, P. M. Oppeneer, U. Nowak, and C. P. Hauri, *Phys. Rev. B* **98**, 014405 (2018).
- [10] H. Lee, C. Weber, M. Fähnle, and M. Shalaby, *Appl. Sci.* **11**, 9753 (2021).
- [11] B. Koopmans, J. J. M. Ruigrok, F. D. Longa, and W. J. M. de Jonge, *Phys. Rev. Lett.* **95**, 267207 (2005).
- [12] K. Carva, M. Battiato, and P. M. Oppeneer, *Phys. Rev. Lett.* **107**, 207201 (2011).
- [13] M. Battiato, K. Carva, and P. M. Oppeneer, *Phys. Rev. Lett.* **105**, 027203 (2010).
- [14] E. Runge and E. K. U. Gross, *Phys. Rev. Lett.* **52**, 997 (1984).
- [15] *Fundamentals of Time-Dependent Density Functional Theory*, edited by M. A. L. Marques, N. T. Maitra, F. M. S. Nogueira, E. K. U. Gross, and A. Rubio (Springer, Berlin/Heidelberg, 2012), pp. 53–99.
- [16] P. Elliott, M. Stamenova, J. Simoni, S. Sharma, S. Sanvito, and E. K. U. Gross, Time-dependent density functional theory for spin dynamics, in *Handbook of Materials Modeling : Methods: Theory and Modeling*, edited by W. Andreoni and S. Yip (Springer, Cham, 2018), pp. 1–26.
- [17] P. Elliott, F. Furche, and K. Burke, in *Reviews in Computational Chemistry*, edited by K. Lipkowitz and T. Cundari (Wiley, Hoboken, NJ, 2009), Vol. 26, pp. 91–165.
- [18] C. A. Ullrich, *Time-Dependent Density-Functional Theory Concepts and Applications* (Oxford University Press, Oxford, New York, 2011).
- [19] K. Krieger, J. K. Dewhurst, P. Elliott, S. Sharma, and E. K. U. Gross, *J. Chem. Theory Comput.* **11**, 4870 (2015).
- [20] J. K. Dewhurst, A. Sanna, and S. Sharma, *Eur. Phys. J. B* **91**, 218 (2018).
- [21] L. M. Sandratskii and P. G. Guletskii, *J. Phys. F: Met. Phys.* **16**, L43 (1986).
- [22] J. Kubler, K. H. Hock, J. Sticht, and A. R. Williams, *J. Phys. F: Met. Phys.* **18**, 469 (1988).
- [23] J. P. Perdew and Y. Wang, *Phys. Rev. B* **45**, 13244 (1992).
- [24] P. Elliott, T. Müller, J. K. Dewhurst, S. Sharma, and E. K. U. Gross, *Sci. Rep.* **6**, 38911 (2016).
- [25] The ELK FP-LAPW Code, <http://elk.sourceforge.net>.
- [26] J. K. Dewhurst, K. Krieger, S. Sharma, and E. K. U. Gross, *Comput. Phys. Commun.* **209**, 92 (2016).
- [27] D. J. Singh and L. Nordström, *Planewaves, Pseudopotentials, and the LAPW Method* (Springer, Boston, MA, 2006).
- [28] A. L. Chekhov, Y. Behovits, J. J. F. Heitz, C. Denker, D. A. Reiss, M. Wolf, M. Weinelt, P. W. Brouwer, M. Münzenberg, and T. Kampfrath, *Phys. Rev. X* **11**, 041055 (2021).

- [29] K. Momma and F. Izumi, *J. Appl. Crystallogr.* **44**, 1272 (2011).
- [30] J. Chen, U. Bovensiepen, A. Eschenlohr, T. Müller, P. Elliott, E. K. U. Gross, J. K. Dewhurst, and S. Sharma, *Phys. Rev. Lett.* **122**, 067202 (2019).
- [31] K. Krieger, P. Elliott, T. Müller, N. Singh, J. K. Dewhurst, E. K. U. Gross, and S. Sharma, *J. Phys.: Condens. Matter* **29**, 224001 (2017).
- [32] F. Siegrist, J. A. Gessner, M. Ossiander, C. Denker, Y.-P. Chang, M. C. Schröder, A. Guggenmos, Y. Cui, J. Walowski, U. Martens, J. K. Dewhurst, U. Kleineberg, M. Münzenberg, S. Sharma, and M. Schultze, *Nature (London)* **571**, 240 (2019).
- [33] M. Krauß, T. Roth, S. Alebrand, D. Steil, M. Cinchetti, M. Aeschlimann, and H. C. Schneider, *Phys. Rev. B* **80**, 180407(R) (2009).
- [34] A. Marini, *J. Phys.: Conf. Ser.* **427**, 012003 (2013).